

# Role of orthopyroxene in rheological weakening of the lithosphere via dynamic recrystallization

Robert J. M. Farla<sup>1,2</sup>, Shun-ichiro Karato, and Zhengyu Cai

Department of Geology and Geophysics, Yale University, New Haven, CT 06511

Edited by David L. Kohlstedt, University of Minnesota, Minneapolis, MN, and approved September 3, 2013 (received for review October 19, 2012)

**For plate tectonics to operate on a terrestrial planet, the surface layer (the lithosphere) must have a modest strength (Earth,  $\leq 200$  MPa), but a standard strength profile based on olivine far exceeds this threshold value. Consequently, it is essential to identify mechanisms that reduce the strength of the lithosphere on Earth. Here we report results of high-strain laboratory deformation experiments on a representative olivine–orthopyroxene composition that show the addition of orthopyroxene substantially reduces the strength in the ductile regime within a certain temperature window. The reduction in strength is associated with the formation of small orthopyroxene and olivine grains. Our samples show heterogeneous microstructures similar to those observed in natural peridotites in shear zones: fine-grained regions containing both orthopyroxene and olivine that form interconnected bands where a large fraction of strain is accommodated. A model is developed to apply these results to geological conditions. Such a model, combined with our experimental observations, suggests that orthopyroxene may play a key role in the plastic deformation of the lithosphere in a critical temperature range, leading to long-term weakening associated with strain localization in the lithosphere.**

rheology | two-phase | Zener pinning | deformation mechanisms | electron probe microanalysis

Plate tectonic style of convection is characterized by regions of localized deformation, such as subduction zones, and the origin of these regions needs to be investigated to understand why plate tectonics operates on Earth. Localized deformation at plate boundaries involves not only brittle fracture at shallow portions but also localized deformation in the ductile shear zones (1–4). Although the basic processes of localized deformation in the brittle regime are well understood (5, 6), mechanisms of localized deformation in the ductile regime remain elusive. The strength profile of the lithosphere in a standard model (7) predicts stresses that are much higher than the critical strength below which plate tectonic style of convection would occur (8, 9).

Among the possible mechanisms of shear localization (10), grain size reduction is most often recognized in ductile shear zones and has been given particular attention in previous studies (11–15). Grain size reduction can occur during high-temperature deformation by dynamic recrystallization during dislocation creep (16, 17). In many cases, small grains are formed along preexisting grain boundaries (18). If the degree of grain-size reduction is large enough and these fine-grained regions are connected, then regions of small grain size will be deformed by grain-size-sensitive creep processes—diffusion creep or dislocation creep accommodated by grain-boundary sliding (Dis-GBS) introduced by Hirth and Kohlstedt (1995) (19). Deformation in both regimes results in the weakening of a rock, although less so in the Dis-GBS regime. In addition, for this weakening to cause substantial shear localization, the influence of grain growth must be minimal. Pinning of grain boundaries by a second phase is an obvious possibility, and therefore it is essential to understand the microstructural development during deformation of multi-phase rocks. One of the key observations in naturally deformed peridotitic rocks in shear zones is the association of degree of mixing with localization: well-developed shear zones (mylonites,

ultramylonites) are in most cases comprised of a well-mixed mineralogy with smaller grain size and larger volume fraction of secondary phases (3).

Previous theoretical studies have addressed various shear localization processes (20, 21). However, experimental studies are essential to make further progress in this area because the essence of shear localization is the development of heterogeneous microstructure that is difficult to be captured by theoretical studies. In this article, we describe experimental observations on the microstructural development and mechanical behavior of olivine + orthopyroxene aggregates, and we present a theoretical model to interpret the results and extrapolate them to geological conditions.

Using a Griggs apparatus, we conducted deformation experiments on hot-pressed olivine (75%) and orthopyroxene (25%) aggregates in nearly simple-shear geometry at pressures between 1.3 and 2.0 GPa and temperatures between 1,173 and 1,540 K (Fig. 1). Deformation is nearly simple shear because the sample is oriented on the plane in the direction of maximum shear stress (Fig. S1). However, because of the presence of a compressive stress normal to the sample plane, there is always a small ( $<20\%$ ) contribution from axial compression. We deformed samples to shear strains of 0.7–3.0 at constant displacement rates equivalent to strain rates between  $3.5 \times 10^{-5}$  and  $2.3 \times 10^{-4} \text{ s}^{-1}$  (Methods Summary and Materials and Methods).

In experiments at intermediate temperatures (1,373–1,500 K), we observed a progressive increase in shear stress  $\tau$  followed by strain weakening (Fig. 1). Upon termination of the experiments, we observe at 1,373 K  $\sim 38\%$  weakening and observe at 1,473 K

## Significance

The theory of plate tectonics is well established for Earth; however, why it operates is less well known. Here we propose that the deformation of a realistic two-phase aggregate (olivine and orthopyroxene) contributes to the rheological weakening and localization in the lower lithosphere and upper mantle. In particular, in a certain temperature range, the experimentally deformed aggregates show substantial weakening and the partitioning of strain in fine-grained regions composed of both olivine and orthopyroxene, possibly governed by grain-boundary pinning effects. However, at higher temperatures, the polyphase aggregates deform more homogeneously and are subject to less weakening. Using a model, we predict the conditions under which localized deformation may occur in the Earth.

Author contributions: R.J.M.F. and S.-i.K. designed research; R.J.M.F. and Z.C. performed research; S.-i.K. contributed new reagents/analytic tools; R.J.M.F. analyzed data; and R.J.M.F. wrote the paper.

The authors declare no conflict of interest.

This article is a PNAS Direct Submission.

<sup>1</sup>Present address: Bayerisches Geoinstitut, Universität Bayreuth, 95440 Bayreuth, Germany.

<sup>2</sup>To whom correspondence should be addressed. E-mail: robert.farla@uni-bayreuth.de.

This article contains supporting information online at [www.pnas.org/lookup/suppl/doi:10.1073/pnas.1218335110/-DCSupplemental](http://www.pnas.org/lookup/suppl/doi:10.1073/pnas.1218335110/-DCSupplemental).

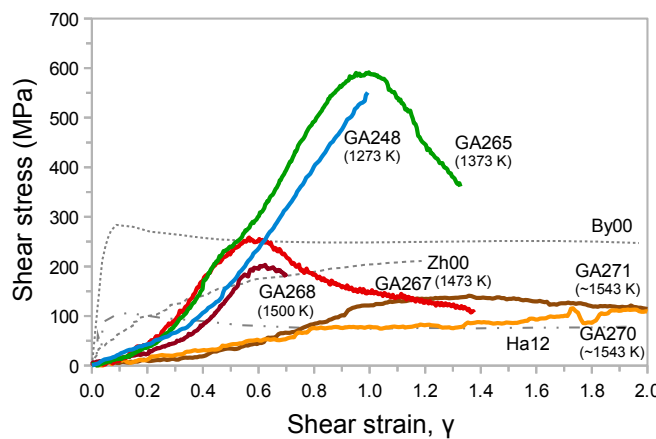


**Fig. 1.** Shear stress–shear strain curves for deformation at constant strain rate on a select number of key experiments. The colored curves correspond to current experiments and are labeled by run number and temperature. The gray curves correspond to deformation of olivine polycrystals at 1,473 K and similar strain rates carried out in nearly simple shear geometry (Zh00,  $\text{Fo}_{90}$ , dashed curve) (22) and in torsional geometry [By00,  $\text{Fo}_{90}$ , dotted curve (23) and Ha12,  $\text{Fo}_{90}$ , dash-dotted curve (24)]. In this study, peak flow stresses were achieved at 1,373 K and higher temperatures.

~60% weakening following the peak stress. In contrast, at low temperatures ( $\leq 1,273$  K), the specimens kept strain hardening. At the highest temperatures ( $> 1,500$  K), no appreciable strain weakening was observed up to shear strains of  $\gamma \sim 3.0$  (GA270/1).

We compare our data for olivine–orthopyroxene aggregates at 1,473 K (Fig. 1) with three previous studies that have explored large strain deformation of polycrystalline olivine, one in nearly simple-shear geometry (22) and two in torsional geometry (23, 24). Overall, we see that the peak strength of our olivine–orthopyroxene mixture is comparable to pure, but dry,  $\text{Fo}_{90}$  olivine aggregates deformed at 1,473 K and similar strain rates ( $\sim 10^{-4} \text{s}^{-1}$ ). Previous studies on  $\text{Fo}_{90}$  olivine show between 0% and 15% weakening after the peak flow stress was reached

(22, 23), whereas  $\text{Fo}_{50}$  shows up to ~50% weakening (24). To be clear, strain weakening does not necessarily suggest localization occurred, and can happen via a range of mechanisms but is generally associated with an overall reduction in grain size.

To investigate how strain weakening occurred in our samples, we conducted microstructural observations using the scanning electron microscope (SEM) and the electron-probe microanalyzer (EPMA). Additional electron backscatter diffraction (EBSD) data is presented in Figs. S2 and S3. Fig. 2 shows the SEM images and element (Si) maps of representative regions of selected specimens deformed at four temperatures. The hot-pressed starting materials show near-uniform distribution of orthopyroxene grains among olivine grains with an average grain size  $\sim 14 \mu\text{m}$ , with near-equilibrium grain-boundary morphology and equant grain shapes (Fig. 2A). However, the deformed microstructures for GA265 and GA267, in particular, show a bimodal grain size distribution characteristic of heterogeneous deformation. In contrast, at  $\sim 1,540$  K, the sample GA270 mostly recrystallized homogeneously (Fig. 2E and J). Dynamic recrystallization is the likely main cause for grain size reduction and weakening. We do not observe much grain-boundary bulging, which suggests most recrystallization occurred via subgrain rotation mechanism (25). Grain shape analysis of some orthopyroxene grains for GA267 suggests plastic strains larger than the average strain of the sample also occurred (Materials and Methods).

By comparing the backscattered electrons images directly with the Si element maps (Fig. 2B–D versus Fig. 2F–H), we observe that for all samples the minerals olivine and orthopyroxene recrystallized, but at different grain sizes. The mixing of recrystallized grains is highlighted in Fig. 2 by yellow regions representing olivine and the pink regions representing orthopyroxene (Fig. S4). The extent of recrystallization depends on temperature and strain, where GA265, GA267, and GA270 have recrystallized to  $\sim 13\%$ ,  $\sim 28\%$ , and  $\sim 71\%$ , respectively (Fig. S5). In the mixed-phase regions of specimens GA265 and GA267, the recrystallized grain size of olivine is somewhat larger than that of orthopyroxene by 10–30%, and the average recrystallized grain size is systematically smaller than the recrystallized grain size of

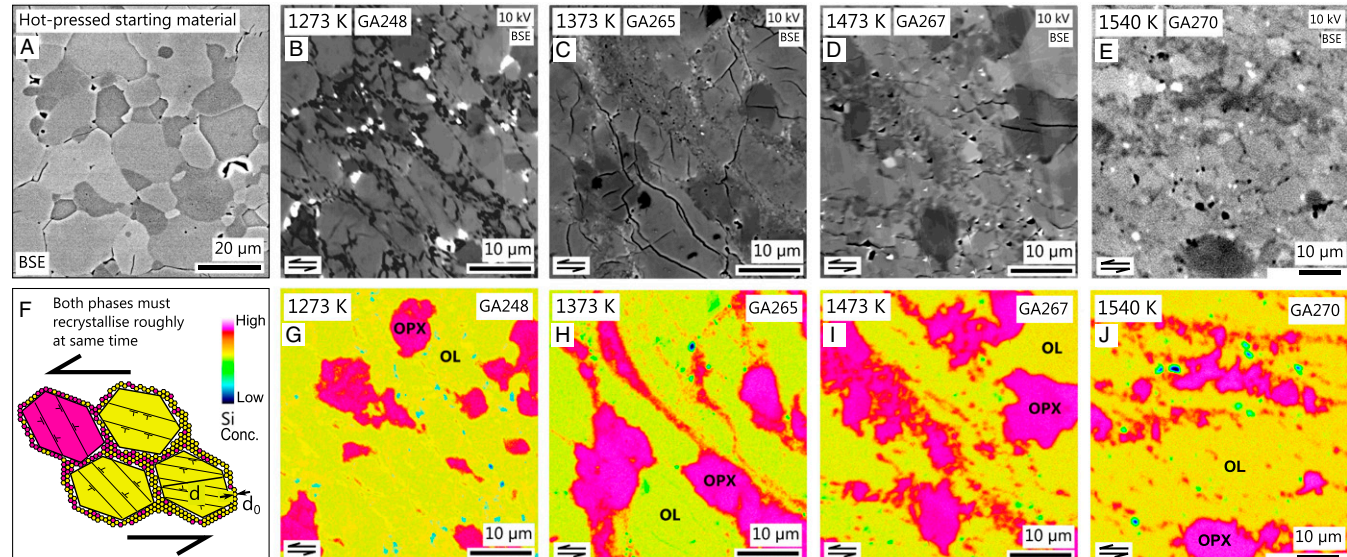


**Fig. 2.** Backscattered electron images and microprobe Si element maps showing a hot-pressed microstructure (A) and deformation microstructures at a series of temperatures: 1,273 K (B), 1,373 K (C), 1,473 K (D), and 1,540 K (E). Dark shaded grains are generally orthopyroxene and correspond to the pink shaded regions in the Si element maps (G–J), whereas the yellow regions correspond to olivine grains. The cartoon in F highlights the principle behind recrystallization and mixing of new grains under an applied shear strain. Recrystallized grain size,  $d_0$ , typically increases with stress as described by a paleo-piezometer (26).

**Table 1.** Deformation run parameters and specimen analysis

Run no.	P, T, GPa, K	Shear strain, $\gamma$	Shear rate, $s^{-1}$	Shear stress, $\tau$ , MPa*	Water content before/after, wt. ppm H <sub>2</sub> O†	Initial grain size, d, $\mu\text{m}^‡$	Recrystallized grain size, $d_0$ , polyphase olivine/oxp, $\mu\text{m}^‡$	Recrystallized grain size, $d_0$ , monophase olivine, $\mu\text{m}^‡$
GA256	1.5, 1,173(20)	—	$\sim 10^{-4}$	604§	54(22)/56 (18)	5(3)	—	—
GA248	1.3, 1,273(20)	1.0	$2.3 \times 10^{-4}$	545§	317(61)/110 (32)	5(3)	ca. 0.3	1.3(0.8)
GA254	1.5, 1,273(20)	0.7	$4.5 \times 10^{-5}$	380§	182(55)/54 (22)	5(3)	—	—
GA258	1.5, 1,373(20)	0.4	$3.5 \times 10^{-5}$	174§	413(74)/119 (26)	15(10)	—	—
GA265	1.5, 1,373(20)	1.3	$1.2 \times 10^{-4}$	590	398(85)/118 (64)	14(9)	0.44(0.20)/ 0.37(0.17)	1.5(0.7)
GA267	2.0, 1,473(20)	1.4	$1.2 \times 10^{-4}$	255	398(85)/96 (18)	14(9)	1.52(0.88)/ 0.96(0.55)	2.8(0.9)
GA268	2.0, 1,498(20)	0.7	$1.1 \times 10^{-4}$	190	398(85)/77 (19)	14(9)	3.36(2.30)/ 2.90(1.00)	5.2(4.2)‡
GA270	2.0, 1,540(50)	3.0	$2.1 \times 10^{-4}$	150§	398(85)/227(67)	14(9)	3.18(1.57)/ 2.78(1.70)	3.0(1.9)‡
GA271	2.0, 1,540(50)	2.1	$2.2 \times 10^{-4}$	140	213(78)/106 (30)	11(9)	—	4.0(1.0)‡

Uncertainty, where given in parentheses, is 1 SD. Opx, orthopyroxene.

\*Shear stress corrected for linear increase in friction and strength of nickel capsule.

†Paterson 1982 calibration.

‡No clear regions of localized deformation developed.

§Shear stress at maximum strain.

olivine in the monophase regions by a factor of  $\sim 2$ –3 (Table 1). In contrast, the olivine and orthopyroxene grain size in the polyphase regions of a recrystallized sample deformed at the highest temperatures (Fig. 2*J*, Fig. S4, and Fig. S5*C*) is more similar to the olivine grain size in the monophase regions (Table 1). Finally, at intermediate temperatures, the fine-grained and mixed-phase regions may be partially interconnected (Fig. 2 *B*–*D* and Fig. S4*D*). Additional connectivity in the third dimension is possible, but only advanced techniques, such as X-ray tomography or Focused Ion Beam milling combined with electron backscatter diffraction (EBSD), may reveal more.

To understand why rheological weakening occurred in a certain temperature range but not for other temperatures, we plot our experimental observations in a deformation mechanism map of olivine (see Table S1 for flow laws used) combined with a recrystallized grain size–stress relationship (26) (Fig. 3). Fig. 3 consists of six panels where the first row of panels (Fig. 3 *A*–*C*) only include dislocation creep and diffusion creep for wet conditions and second row of panels (Fig. 3 *D*–*F*) include an additional deformation mechanism, Dis-GBS (27). We note that Dis-GBS creep may play an important role, but the exact flow laws are poorly constrained, particularly under “wet” conditions. The effect of including this flow law in the deformation mechanism map is that the stress predicted (for pure olivine) at the onset of our experiments should already be nearly an order of magnitude lower at a constant strain rate of  $\sim 1 \times 10^{-4} \cdot s^{-1}$ . Furthermore, deformation still proceeds into the diffusion creep regime as highlighted by the position of the data points (except at the highest temperature). We emphasize that only in diffusion creep can a rock be truly weakened, an important aspect for the strength evolution of the lithosphere.

Low-temperature experiments ( $\leq 1,273$  K) were terminated before substantial deformation and recrystallization occurred (Table 1, Fig. 2 *B* and *F*), because deformation at lower temperatures ( $T \leq 1,273$  K) required plastic flow stresses to exceed the confining pressure of the experiments potentially leading to the onset of brittle deformation processes. At temperatures above  $\sim 1,273$  K, the recrystallized grain size is increasingly smaller than the critical grain size (Fig. 3 *A* and *B*). In this latter case, rheological weakening is possible. The recrystallized grain sizes (for mixed regions) plotted by the circular symbols in Fig. 3 are systematically smaller than the recrystallized grain sizes in pure olivine (asterisk symbols). Finally, at the highest temperature explored in this study ( $T \sim 1,540$  K), the dynamically recrystallized grain size is close to the critical grain size between diffusion and dislocation creep and not much weakening is observed (Fig. 1).

The essential cause for rheological weakening in our experiments is grain-size reduction. At low temperatures, no appreciable recrystallization occurs, whereas at high temperatures, recrystallized grain size is too large for weakening. In the intermediate temperature range, substantial recrystallization occurs to produce small enough grains (Fig. 2 and Fig. S4). The detailed microstructural analyses show that samples deformed at intermediate temperatures develop heterogeneous microstructures, and large strains in some of the favorably oriented grains (expressed by the Schmid factor) that experienced a large degree of recrystallization (Fig. S6). The local strain was determined from the shape of grains (circularity), assuming the initial shape of each grain was circular (Materials and Methods). We find large variability in grain shapes of parent orthopyroxene grains. The highly elongated (orthopyroxene) grains typically develop long tails or bands composed of small grains that presumably recrystallized from the elongated parent grain(s). Local strain in these recrystallized regions can therefore be much larger than the macroscopically imposed strain. Large strains provide an effective mechanism of grain mixing through grain-switching events (28). Evidence for Zener pinning is also found, suggesting the importance of mixing to maintain small grain size (Materials and Methods and Fig. S7).

Our laboratory results are obtained at much higher stresses (strain rates) than those operating in Earth. Consequently, we need to understand the conditions for weakening based on a physical model and use that model to extrapolate the results to the Earth's interior. Let us consider a case where stress suddenly increases (this could be due to bending of lithosphere at a trench). Upon the increase in stress, new small grains will be formed at preexisting grain boundaries. If the size of these newly formed grains is smaller than the previously discussed critical grain size, then rheological weakening associated with localization will occur. However, in those regions where diffusion creep takes over, dynamic recrystallization ceases and grain growth follows. If grain growth is fast, then no substantial deformation occurs in the fine-grained regions. Therefore, grain growth must be slow enough to allow for the accumulation of large strains in fine-grained regions. Such a concept was formulated by Karato (2008, chap. 16) (29), where he characterized the conditions for localized deformation using two parameters. One corresponds to the relation between recrystallized grain size and the critical grain size for transition between diffusion and dislocation creep. Another is a parameter expressing the competition between deformation and grain growth (Materials and Methods). Karato (2008) also discussed that in pure olivine, grain growth is so fast that shear localization will not occur.

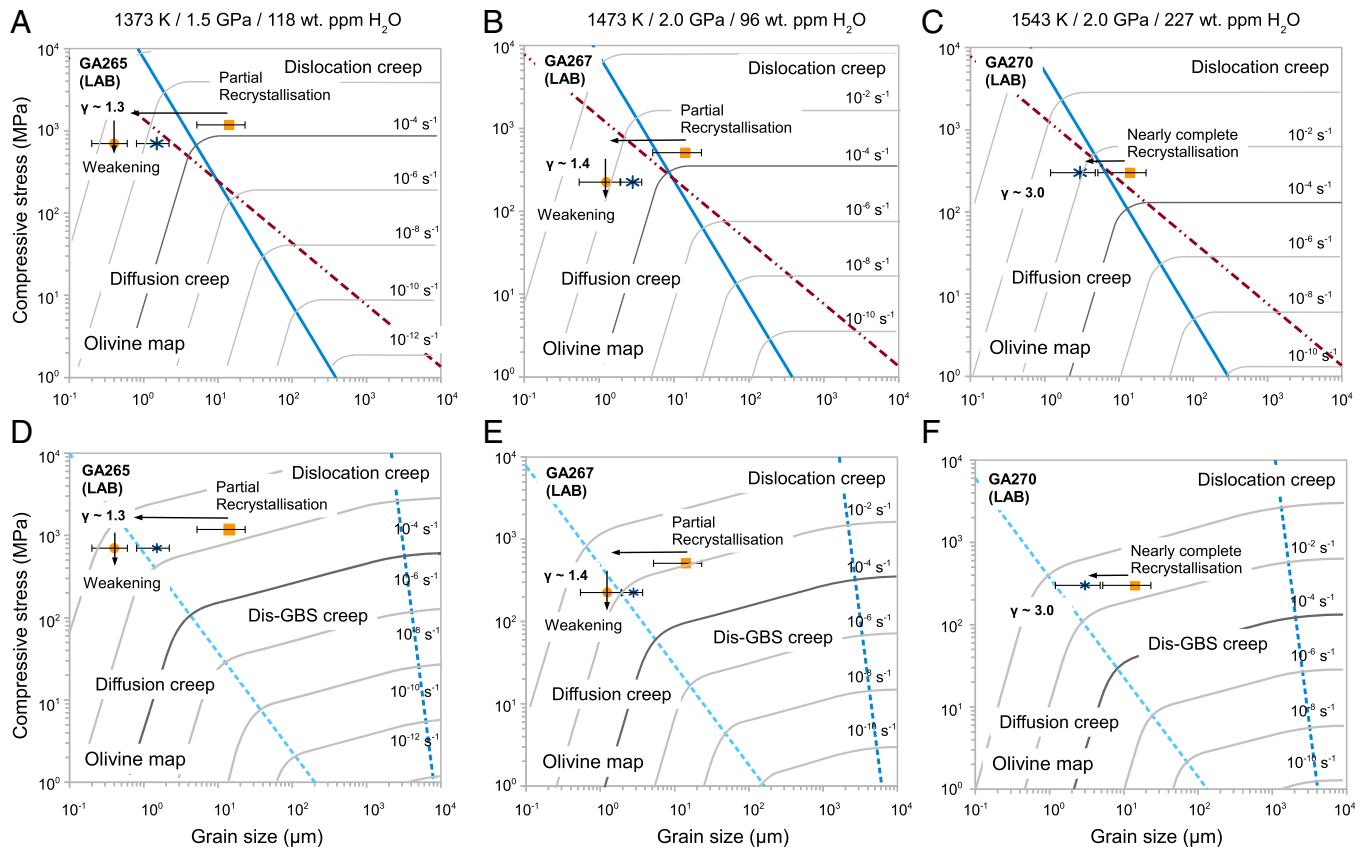


**Fig. 3.** Deformation mechanism maps based on empirical wet olivine flow laws (Table S1) corresponding to three different temperatures at which specimens GA265, GA267, and GA270 were deformed. Stresses are recalculated for compressional geometry,  $\sigma$  (stress) =  $2\tau$  (shear stress). The solid blue line indicates the boundary between diffusion and dislocation creep regimes, the gray lines are constant strain rate contours (labeled), and the purple dashed line is the paleopiezometer for olivine (26). In A–C we used the flow laws for diffusion creep and dislocation creep in wet olivine, whereas in D and E we added an additional deformation mechanism: Dislocation accommodated grain-boundary creep (Dis-GBS) (Table S1). In each deformation mechanism map (A–F) two to three data points are plotted as follows: peak flow stress for original hot-pressed grain size (orange square), flow stress at maximum shear strain in mixed-phase regions (orange circle), and olivine-only regions (blue asterisk). Note that for GA270, no true mixed-phase regions could be identified. The arrows indicate the path of microstructural evolution.

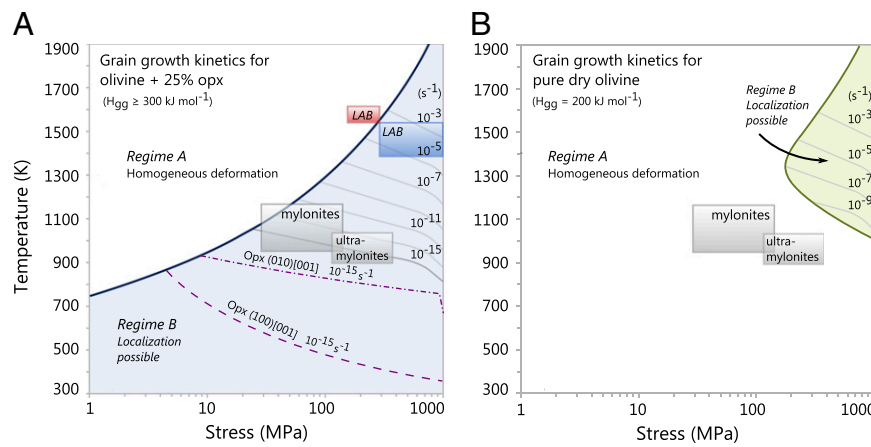
The presence of a secondary phase slows down the kinetics of grain growth due to Zener pinning. As a result, a secondary phase reduces the dynamically recrystallized grain size. These effects enhance the degree of rheological weakening and promote localization. We use a preliminary dataset on the grain-growth kinetics in an olivine + protoenstatite aggregate (30), but the data given on the influence of secondary phase on the size of recrystallized grains of a primary phase are limited to a narrow range in grain size (0.6–2.9  $\mu$ m); thus, we only offer qualitative discussions on this effect.

Fig. 4 shows the conditions for shear localization with grain-growth kinetics included for both olivine + orthopyroxene mixture and olivine alone. Unlike in Fig. 3, we used the flow laws for dry olivine (Table S1) to calculate the boundaries in Fig. 4 (*Materials and Methods*) because two-phase grain-growth measurements are only available for dry conditions, the flow laws for the relevant deformation mechanisms are better constrained for dry conditions, and typically the lithosphere is assumed to be (nearly) dry. We constructed this figure by translating the variables in the Karato model (29) from two nondimensional parameters to temperature and stress. In this figure, the maximum temperature at which substantial localization associated with weakening can occur corresponds to the condition where recrystallized grain size falls inside the diffusion creep regime. The low temperature limit shown for pure olivine corresponds to the temperature above which grain-growth kinetics is too fast

compared with diffusion creep (using parameters in Table S2). This lower temperature limit does not exist for an olivine-orthopyroxene mixture with very slow grain-growth kinetics.

The model based on the experimental data on olivine + orthopyroxene grain-growth kinetics (30) agrees with observations from this experimental study and with observations of natural peridotites deformed under lower temperature and strain rate conditions (Fig. 4A). Furthermore, the observed efficient mixing of recrystallized olivine and orthopyroxene grains in our study is consistent with the microstructures observed in sheared peridotites (2, 3), suggesting that our observations and model offer a reasonable means of assessing the potential for shear weakening across a range of temperature–stress–strain rate conditions.

However, natural observations are inconsistent with a model prediction based on pure olivine grain-growth kinetics (29) (Fig. 4B). Therefore, we conclude that the pure olivine model of the lithosphere alone cannot explain shear localization in the lithosphere. In addition, our experimental observations are considerably different from those on pure olivine under similar conditions (22, 23). Bystricky et al. (2000) (23) observed only modest strain weakening (~10%) associated with nearly homogeneous recrystallized microstructure. We show that the presence of orthopyroxene results in a highly heterogeneous microstructure and that the recrystallized grain size in mixed regions is smaller than in unmixed regions (Table 1). Therefore,



**Fig. 4.** Model describing the regimes for homogeneous deformation and strain localization in temperature–stress space. In both regimes, various amounts of rheological weakening are possible by different mechanisms, but long-term weakening is possible once the strain has fully localized. The model is based on dry olivine flow laws (Table S1), a paleopiezometer (26), and olivine (+orthopyroxene) grain-growth kinetics (Table S2) (30). The gray lines (olivine) and purple dashed lines (orthopyroxene) (36) are constant strain rate contours for deformation in the dislocation creep and transition to Peierls (high stress) creep regimes (where shown by an inflection point in the curve). Panel A shows a large regime where localization is possible, including the temperature–stress space for geological conditions for mylonite and ultramylonite formation. This regime exists only when the grain-growth kinetics is controlled by a given volume fraction of 25% orthopyroxene with Zener pinning grain size exponent of 4 and activation energies of  $300 \text{ kJ mol}^{-1}$  or higher. Panel B demonstrates that development of a heterogeneous microstructure in pure olivine with fast grain-growth kinetics ( $H_{gg} \sim 200 \text{ kJ mol}^{-1}$ ) (29) is restricted to certain laboratory conditions only.

we interpret that the difference is mainly caused by the role of orthopyroxene in the dynamically recrystallizing mixture.

More recent experiments on polycrystalline  $\text{Fo}_{50}$  olivine at 1,473 K (i.e., higher homologous temperature of  $0.78 \text{ T/T}_m$ ) show that this olivine type deformed homogeneously under constant strain rate conditions with 25–50% weakening after peak stress (24, 31). Hansen et al. (2012) (31) suggested that such amount of weakening was possible via both recrystallization and development of a strong lattice preferred orientation (LPO) in their microstructure, the latter lacking in our study (*Materials and Methods*). Even though a stress reduction up to a factor of 2 is possible in pure olivine deformed to large strains ( $\gamma \sim 10$ ), we infer that the polyphase aggregates weaken more efficiently at smaller strains due to a switch in deformation mechanism and sluggish dynamic grain growth. In the long term, recrystallized grains in pure olivine will quickly recover to larger sizes, whereas recrystallized grains in a polyphase mixture persist, likely over geological time, enabling deformation to remain localized.

Considerable weakening associated with mixed-phase dynamic recrystallization observed in our experiments helps to explain the weakness of the oceanic lithosphere on Earth implied by the operation of plate tectonics. The similarity in microstructure between our samples in the laboratory and naturally deformed peridotites in shear zones suggests that similar physical processes may operate in these two cases. However, application of our results to explain the presence or absence of plate tectonics on various planets is not straightforward. First, although the physical mechanisms and conditions for localization are well constrained by our study, a quantitative estimate of the degree of weakening is difficult. Studies, such as the one by Montési (2013) (32) on modeling the distribution and interconnectivity of a network of shear zones, are needed to estimate the magnitude of rheological weakening in the lithosphere. Our results provide a critical dataset for such modeling. Second, our samples contain a small amount of water (Fig. S8 and *Materials and Methods*). Although we were unable to measure water content in olivine and orthopyroxene grains individually, due to too small recrystallized grain size, orthopyroxene is known to take in more water than olivine under lithospheric pressures (<9 GPa) (33). It is likely that a small amount of water enhances the rate of

deformation and recrystallization of orthopyroxene as it does for olivine and quartz (24, 35). Furthermore, higher water content may lead to larger or smaller recrystallized grains, depending on the competition between nucleation and growth kinetics affected by water. The outcome may therefore prevent a switch in deformation mechanism if the recrystallized grain sizes of different phases are too large or if nucleation-growth kinetics of different phases is too different. The influence of water on deformation of olivine–orthopyroxene mixtures is currently unknown and open for further investigation.

## Methods Summary

For a detailed methodology, see *Materials and Methods*. San Carlos olivine and orthopyroxene grains were hand-picked for gem quality, crushed to micrometer grain size, and ultrasonically mixed for 75% olivine–25% orthopyroxene weight composition. The powders were left in laboratory air (~30% humidity) to ensure grain growth during hot pressing. A Griggs-type solid-medium apparatus was used both for hot isostatic pressing of the olivine–orthopyroxene mixture and for deformation with a soft caesium chloride (CsCl) pressure medium (Fig. S1). A typical hot-press experiment was carried out at 1,573 K for 7 h at 1.3 GPa using nickel as capsule material to control oxygen fugacity. After quenching and depressurisation, the recovered hot-pressed material was cut into slices at 45° with a diamond blade, leaving some material for microstructural analysis and water content measurement. Procedures for deformation closely follow those described by Ohuchi et al. (2011) (36) with the following modifications. Each specimen slice was cut in half for a nickel foil strain marker and sandwiched at 45° between two grooved alumina pistons inside a nickel capsule. The loaded capsule was placed inside the Griggs solid-salt (CsCl) deformation cell and pressurized and heated to target conditions ( $P = 1.3\text{--}2.0 \text{ GPa}$ ;  $T = 1,173\text{--}1,540 \text{ K}$ ). At target conditions, nearly simple shear deformation experiments were carried out at constant strain rate (typically  $\sim 10^{-4} \text{ s}^{-1}$ ). At the highest temperatures (~1,540 K) and pressures (2 GPa), temperature was estimated from the power–temperature relationship with an uncertainty of 50 K as the thermocouples repeatedly failed under these conditions. The deformed specimens were recovered, polished, and analyzed for water content (FTIR spectroscopy) and microstructure using the SEM with EBSD and EPMA.

**ACKNOWLEDGMENTS.** We thank Take Hiraga and Miki Tasaka for the data on grain-growth kinetics in the olivine + pyroxene mixture. The manuscript was substantially improved by three reviewers. This research was supported by grants from the National Science Foundation.

1. Warren JM, Hirth G (2006) Grain size sensitive deformation mechanisms in naturally deformed peridotites. *Earth Planet Sci Lett* 248(1-2):423–435.
2. Toy VG, Newman J, Lamb W, Tikoff B (2010) The role of pyroxenites in formation of shear instabilities in the mantle: Evidence from an ultramafic ultramylonite, Twin Sisters masif, Washington. *J Petrol* 51(1-2):55–80.
3. Linckens J, Herwegh M, Müntener O, Mercalli I (2011) Evolution of a polymimetic mantle shear zone and the role of second phases in the localization of deformation. *J Geophys Res* 116:B06311, 10.1029/2010JB008119.
4. Drury MR, Vissers RLM, Van der Wal D, Hoogerduijn Strating EH (1991) Shear localisation in upper mantle peridotites. *Pure and Applied Geophysics PAGEOPH* 137(4): 439–460.
5. Chernak LJ, Hirth G (2010) Deformation of antigorite serpentine at high temperature and pressure. *Earth Planet Sci Lett* 296:23–33.
6. Paterson MS, Wong T-F (2005) *Experimental Rock Deformation—The Brittle Field* (Springer, Berlin).
7. Kohlstedt DL, Evans B, Mackwell SJ (1995) Strength of the lithosphere: Constraints imposed by laboratory experiments. *J Geophys Res* 100(B9):17587–17, 602.
8. Tackley PJ (2000) Self-consistent generation of tectonic plates in time-dependent, three-dimensional mantle convection simulations. *Geochem Geophys Geosyst* 1(8):1021.
9. Richards MA, Yang W-S, Baumgardner JR, Bunge H-P (2001) Role of a low-viscosity zone in stabilizing plate tectonics: Implications for comparative terrestrial planetology. *Geochem Geophys Geosyst* 2(8):1026.
10. Poirier JP (1980) Shear localization and shear instability in materials in the ductile field. *J Struct Geol* 2:135–142.
11. White SH, Burrows SE, Carreras J, Shaw ND, Humphreys FJ (1980) On mylonites in ductile shear zones. *J Struct Geol* 2(1-2):175–187.
12. Platt JP, Behr WM (2011) Grainsize evolution in ductile shear zones: Implications for strain localization and the strength of the lithosphere. *J Struct Geol* 33(4):537–550.
13. Precigout J, Gueydan F, Gapais D, Garrido CJ, Essaifi A (2007) Strain localisation in the subcontinental mantle—A ductile alternative to the brittle mantle. *Tectonophysics* 445(3-4):318–336.
14. Raimbouy H, Toyoshima T, Harima Y, Kimura G (2008) Grain-size reduction mechanisms and rheological consequences in high-temperature gabbro mylonites of Hidaka, Japan. *Earth Planet Sci Lett* 267(3-4):637–653.
15. Rutter EH, Brodie KH (1988) The role of tectonic grain size reduction in the rheological stratification of the lithosphere. *Geol Rundsch* 77(1):295–308.
16. Karato S, Toriumi M, Fujii T (1980) Dynamic recrystallization of olivine single crystals during high-temperature creep. *Geophys Res Lett* 7(9):649–652.
17. Drury MR (2005) Dynamic recrystallization and strain softening of olivine aggregates in the laboratory and the lithosphere. *Geological Society Special Publications* 243:143–158.
18. Guillope M, Poirier JP (1979) Dynamic recrystallization during creep of single-crystalline halite: An experimental study. *J Geophys Res* 84(B10):5557–5567.
19. Hirth G, Kohlstedt DL (1995) Experimental constraints on the dynamics of the partially molten upper mantle 2. Deformation in the dislocation creep regime. *J Geophys Res* 100:15,441–15,449.
20. Rozel A, Ricard Y, Bercovici D (2011) A thermodynamically self-consistent damage equation for grain size evolution during dynamic recrystallization. *Geophys J Int* 184(2):719–728.
21. Bercovici D, Ricard Y (2012) Mechanisms for the generation of plate tectonics by two-phase grain-damage and pinning. *Phys Earth Planet Inter* 202–203:27–55.
22. Zhang S, Karato S-i, Fitz Gerald J, Faul UH, Zhou Y (2000) Simple shear deformation of olivine aggregates. *Tectonophysics* 316(1-2):133–152.
23. Bystricky M, Kunze K, Burlini L, Burg JP (2000) High shear strain of olivine aggregates: Rheological and seismic consequences. *Science* 290(5496):1564–1567.
24. Hansen LN, Zimmerman ME, Dillman AM, Kohlstedt DL (2012) Strain localization in olivine aggregates at high temperature: A laboratory comparison of constant-strain-rate and constant-stress boundary conditions. *Earth Planet Sci Lett* 333–334(0): 134–145.
25. Drury MR, Pennock GM (2007) Subgrain rotation recrystallization in minerals. *Mater Sci Forum* 550:95–104.
26. Van der Wal D, Chopra P, Drury M, Gerald JF (1993) Relationships between dynamically recrystallized grain size and deformation conditions in experimentally deformed olivine rocks. *Geophys Res Lett* 20(14):1479–1482.
27. Hansen LN, Zimmerman ME, Kohlstedt DL (2011) Grain boundary sliding in San Carlos olivine: Flow law parameters and crystallographic-preferred orientation. *J Geophys Res* 116(B08201).
28. Ashby MF, Verrall RA (1973) Diffusion-accommodated flow and superplasticity. *Acta Metall* 21(2):149–163.
29. Karato S (2008) *Deformation of Earth Materials: An Introduction to the Rheology of Solid Earth* (Cambridge Univ Press, New York).
30. Hiraga T, Tachibana C, Ohashi N, Sano S (2010) Grain growth systematics for forsterite ± enstatite aggregates: Effect of lithology on grain size in the upper mantle. *Earth Planet Sci Lett* 291(1-4):10–20.
31. Hansen LN, Zimmerman ME, Kohlstedt DL (2012) Laboratory measurements of the viscous anisotropy of olivine aggregates. *Nature* 492(7429):415–418.
32. Montési LGJ (2013) Fabric development as the key for forming ductile shear zones and enabling plate tectonics. *J Struct Geol* 50:254–266.
33. Keppler H, Bofan-Casanova N (2006) Thermodynamics of water solubility and partitioning. *Rev Mineral Geochem* 62(1):193–230.
34. Jung H, Karato S-i (2001) Effects of water on dynamically recrystallized grain-size of olivine. *J Struct Geol* 23(9):1337–1344.
35. Hobbs BE (1968) Recrystallization of single crystals of quartz. *Tectonophysics* 6(5): 353–401.
36. Ohuchi T, Karato S, Fujino K (2011) Strength of single-crystal orthopyroxene under lithospheric conditions. *Contrib Mineral Petrol* 161(6):961–975.

# Supporting Information

Farla et al. 10.1073/pnas.1218335110

## Materials and Methods

**Starting Materials and Sample Preparation.** The starting materials are from San Carlos peridotite. We selected inclusion- and impurity-free olivine and orthopyroxene grains under the optical microscope. We crushed and sieved the grains of each phase separately into fine powders in the range of 1–5  $\mu\text{m}$  grain size with the help of a mortar and pestle, a pulverizer, and finally a sonic sifter. We ultrasonically mixed the powders in ethanol for one ratio of 75% olivine and 25% orthopyroxene by weight and allowed the ethanol to evaporate. We subsequently cleaned the powder mixture in distilled water and dried the powders in the oven at 383 K overnight. We removed the powders from the oven and stored them in laboratory air pending hot isostatic pressing experiments.

A typical hot-press experiment was carried out in a Griggs solid-medium apparatus as follows. We put the powder mixture in a nickel capsule roughly 5 mm in diameter and 11 mm long. The hot-press assembly was nearly identical to the deformation assembly shown in Fig. S1, however the nickel capsule containing the sample was surrounded by MgO. We pressurized to 1.3 GPa without applying a differential stress on the sample. At pressure, we heated the sample by a graphite furnace to 1,573 K for 7–8 h to anneal the powder mixture into a dense rock with a grain size in the range of 10–50  $\mu\text{m}$ . Upon quenching and depressurization, we recovered the cylindrical sample and sectioned it at 45° to produce up to four slices of 400–500  $\mu\text{m}$  thick. The ends, left over from cutting, were used for microstructural analysis and water content determination (see sections entitled Water Content' and Microstructural Analysis).

**Deformation Experiments.** Deformation experiments were carried out using the same Griggs-type solid-medium deformation apparatus. The details of experimental procedures can be found in Ohuchi et al. (2011) (1). Here we reiterate those methods with minor differences. The deformation conditions ranged in temperature between 1,173 K and ~1,543 K and in pressure between 1.3 and 2.0 GPa. Except in two cases, we carried out experiments at the same constant displacement rate (0.074  $\mu\text{m}\cdot\text{s}^{-1}$ ), resulting in similar calculated strain rates of  $\sim 10^{-4}\cdot\text{s}^{-1}$  (Table 1). A soft pressure medium, caesium chloride (CsCl), was chosen to minimize the friction around the piston and sample. We realized during the course of the project that higher temperatures required higher pressures to avoid partially melting the CsCl (Fig. S1). We do not consider the increase in pressure to affect our results on olivine and orthopyroxene deformation.

In detail, for every deformation experiment, we cut a slice of hot-pressed sample material in two on the wire-saw using a 30- $\mu\text{m}$ -thick wire (to avoid sample loss). During assembly of the deformation cell, we put the sample halves on a grooved alumina piston inside a nickel capsule for oxygen fugacity control. We carefully placed a nickel foil strain marker between the sample halves and sandwiched the sample with another grooved alumina piston on top (Fig. S1). We then sealed the nickel capsule, with the sample inside, using a precision welder. The capsule was placed inside the deformation cell with two Pt/Rh (type R) thermocouples terminating near it (Fig. S1). The temperature difference measured by the upper thermocouple at the center of the sample relative to the lower thermocouple was about 40 K. Once the deformation cell was installed inside the pressure cylinder, we increased the pressure to the desired value in about 2 h followed by an increase in temperature at  $\sim 23\text{ K}\cdot\text{min}^{-1}$ . We annealed the sample at target temperature for half an hour,

followed by the steady advancement of the central piston to generate a differential stress. To find the hit point of the sample, we initially advanced the piston at a higher rate to displace the majority of the CsCl salt between the alumina pistons. We subsequently changed the displacement rate to the desired value for deformation, while the remaining salt was squeezed out and the hit point was recorded. The slope of the displacement versus time record up to the hit point recorded the linear increase in friction during the experiment and was used to determine the final "hit point" of the sample (1).

The shift in peak stress position with strain among experiments shown in Fig. 1 may suggest variable compliance of the apparatus (and/or deformation cell) [see, e.g., Hansen et al. 2011 (2)]. The initial part of a stress-strain curve corresponds to the stiffness of the sample (+ apparatus). The "apparatus" contribution includes machine stiffness + elastic strength of the sample assembly. Indeed, our results show that this apparent stiffness changes with temperature. If the lack of weakening is mainly due to the influence of stiffness, then such an observation is a technical artifact. However, we believe that it is not an artifact because the lack of weakening at the highest temperature and the presence of weakening at 1,373–1,500 K correspond, respectively, to nearly homogeneous microstructures and highly heterogeneous microstructures.

The uncertainties in the measurements were as follows. For strain rate, the uncertainty was about 10–15%, and for temperature, the uncertainty was about 20 K with thermocouples and ~50 K without thermocouples (from power–temperature relationship). The shortening strains were between 11% and 33%. The shear strains were measured from the rotation of the strain marker with about 15% uncertainty due to the irregularity of the shape of the strain marker. The Griggs apparatus contains an inherent uncertainty in the stress measurement even after corrections for linear increase in friction with displacement and strength of nickel are applied. Recently, a comparison was made between deformation in a gas apparatus and the Griggs apparatus, and a systematic offset was found between the two types of stress measurements (3). Unfortunately, the deformation cell and choice of salt as pressure medium were different from our setup, and thus we did not apply this stress correction to our data. We do not place great emphasis on absolute stress measurements and therefore leave the results as they are, open to future reanalysis.

**Water Content.** We used FTIR spectroscopy to measure water contents in our samples, before and after deformation. We carried out the measurements at a resolution of 4  $\text{cm}^{-1}$  with an aperture of  $100 \times 100 \mu\text{m}^2$  in dry air on a KBr plate using a Varian 600 UMA FTIR spectrometer. We captured IR spectra with an unpolarized IR beam in five or more locations on the sample. We characterized the spectra of the doubly polished ~100- $\mu\text{m}$ -thick samples by a broad absorption band of OH-related species in pores, inclusions, and possibly in small melt fractions in triple grain junctions. We observed a few structural OH peaks in the broad absorption band of the wettest specimens (Fig. S8). We applied two corrections to the IR beam absorption in the range of wave numbers 3,000–3,750  $\text{cm}^{-1}$ , a background correction and a baseline correction. We measured the background absorbance after every sample measurement. The background correction is thus given as the difference between the two measurements. We applied the baseline correction by fixing points along the background-corrected IR spectrum except in the range of 3,000–3,750  $\text{cm}^{-1}$ . Finally, we used the Paterson

(1982) (4) calibration to calculate the bulk amount of H<sub>2</sub>O present. The FTIR results are given in Table 1. Unfortunately, we could not measure the water content in individual olivine and orthopyroxene grains due to the small recrystallized grain size.

**Microstructural Analysis. Methodology.** We investigated the microstructures of the hot-pressed and deformed samples by scanning electron microscopy (SEM) imaging, by microprobe analysis with element mapping capability, and by electron backscatter diffraction (EBSD) mapping. A FEI XL-30 series E-SEM at Yale University allowed us to image grains in stage-tilted (70°) secondary electrons (SEs) mode. Tilting the stage accentuates the grain shapes in SE mode. For technical reasons orientation contrast mode at 70° tilt did not provide enough contrast between grains (different shades of gray corresponding to different orientations). We also analyzed areas in backscattered electrons (BSEs) imaging mode to differentiate light-shaded olivine grains from dark-shaded orthopyroxene grains (e.g., Fig. 2, Fig. S6, and Fig. S7). The grain size was determined from a combination of the SE and BSE images of same areas (see, e.g., Fig. S7 A and B). We manually traced grain outlines using image processing software yielding 2–3 grain-boundary maps for each sample (typically near 400 grains per map) at high and low magnification to determine large and small grain size populations accurately. In each map, the grains were analyzed for surface area of discrete particles. The measured grain size is given as the geometric mean of the diameters of circles of equivalent area to each grain in the aggregate. We applied a sectioning bias correction for spheres (multiplication factor of 4/π) to estimate the final 3D grain size.

We carried out microprobe element mapping on areas of 60 × 60 μm<sup>2</sup> using energy dispersive spectroscopy (EDS) and wavelength dispersive spectroscopy (WDS). The acceleration voltage was 10 kV, and we used a step size of 0.04 μm and dwell times of 50 ms for mapping. We analyzed the elements Al, Ca, Fe, Ni, and Si with WDS and Cl, Cs, and Mg with EDS. Fig. 3 shows the Si maps, which displayed the best contrast between olivine and orthopyroxene grains.

We determined the orientations of individual grains using EBSD at an accelerating voltage of 20 kV (Fig. S4). The stage was tilted to 70° to give a working distance of 20 mm, and we chose an objective aperture of 40 μm. We collected diffraction patterns using an HKL Nordlys camera for every 1 μm covering an area of about 220 × 200 μm<sup>2</sup>. Finally, we produced pole figures for several samples (Fig. S3), for the two grain size fractions of olivine and orthopyroxene, where possible.

**Detailed microstructural analysis.** A heterogeneous microstructure in fine-grained regions gives an indication of deformation localizing, but like previous studies on natural shear zones (5–7) the transition from dynamic recrystallization to phase mixing is unclear. This issue can be addressed with additional microstructural analysis. We used three different approaches: (i) we show a tentative relation between grain shape and favorable orientation of grain to shear direction (defined by Schmid factor) in orthopyroxene (Fig. S6); (ii) we show the recrystallized grain size of orthopyroxene, relative to that of olivine in the mixed regions for the samples GA265 and GA267, is favorable for Zener pinning (8) (Fig. S7); and (iii) we emphasize that we locally observe very high strains in some samples with extensive fine-grained bands (Fig. S4) and large embedded orthopyroxene grains deformed to shear strains higher than the bulk strain introduced ( $\gamma \sim 1.4$ ).

The relation between orthopyroxene grain shape [defined by circularity as  $4\pi(\text{Area}/\text{Perimeter}^2)$ ] and the Schmid factor is important because it suggests favorable orientations favor subgrain formation that in turn enhances recrystallization by subgrain rotation. In brief, if a slip system in a grain is oriented very favorably to the stress direction to activate, the Schmid factor is

high, and given geometrical considerations, the grain will likely not be favorably oriented for other slip systems. Fig. S6 shows plots of grain shape (circularity) against Schmid factor for two populations of grains, extensively recrystallizing grains and unrecrystallized grains, measured for sample GA267 using EBSD techniques and image analysis. The recrystallizing grains that are surrounded by a high number of daughter grains have high Schmid factors for either one of the three possible slip systems in orthopyroxene. The grains that appear unaffected by deformation and recrystallization are least favorably oriented for slip. That is, these grains have a low Schmid factor for the weakest slip system in orthopyroxene, (100)[001].

Furthermore, these observations are supported by EBSD analysis of a region in GA267 shown in Fig. S4 D–F. Purple grains are orthopyroxene grains with high Schmid factor for the slip system indicated in the respective legends, and are characterized by subgrain formation and recrystallized tails. In contrast, the large blue orthopyroxene grains have low Schmid factor for the respective slip systems, and appear to have resisted subgrain formation and recrystallization. In Fig. S4 D–F, it would appear that orthopyroxene recrystallization starts at parent orthopyroxene grains, not elsewhere at olivine grain boundaries via some chemical reaction (cf. sketch in Fig. 2E). Finally, one must be careful with this analysis because some grains that were previously in an easy orientation for deformation could have rotated into a hard orientation. In addition, our analysis assumes a homogeneous stress distribution in an aggregate, which is unlikely.

Fig. S7 demonstrates that Zener pinning is a distinct possibility for the fine-grained and mixed regions found in samples GA265 and GA267 (Fig. S4), and less so for samples GA268, deformed to small strain, and GA270, deformed at the highest temperature (Fig. S4C, Fig. S2). To obtain this result, we carried out grain size analysis by imaging representative areas using both SE and BSE mode. The stage was tilted 70° in SE mode to enhance the grain topography. An example of an area of a sample is shown in Fig. S7 A and B using these imaging modes. We confirmed the dark regions (i.e., grains) are orthopyroxene by using EDS. The light-gray grains are olivine. The grain boundaries were then traced by hand. For selected samples, we also added EBSD map images to the grain size analysis for each mineral phase. In the images, we identified recrystallized regions of phase mixing and recrystallized regions of single phase (olivine), as shown in Fig. S7B. These regions were analyzed separately for grain size using image processing software (ImageJ) to arrive at the data plotted in Fig. S7 C and D. We observe a trend of higher orthopyroxene volume fraction ( $f_{\text{opx}}$ ) with smaller grain sizes of both phases in the mixed-phase regions than in the monophase regions. Following Linckens et al. (2011) (5), we plot the olivine grain size ( $D_{\text{ol}}$ ) against the Zener factor ( $d_{\text{opx}}/f_{\text{opx}}$ ) and identify two slopes shown by dash-dotted curves. For small  $z$  values, deformation in the mixed-phase regions is controlled by the “second phase,” and for larger  $z$  values, deformation is controlled by recrystallization processes. Note that the dash-dotted curves are only indicative where the effect of temperature (and stress) on grain size is ignored. Roughly speaking, larger values of  $D_{\text{ol}}$  are predicted at higher temperatures (lower stress), and smaller values of  $D_{\text{ol}}$  are predicted at lower temperatures (higher stress). Not enough data are available to show these trends.

Thus far, we have established the following: a mechanism for recrystallization of orthopyroxene (and olivine), not all orthopyroxene grains recrystallize to the same extent depending on their orientation, and Zener pinning is most effective in samples that deformed heterogeneously at moderate temperatures. We suggest the following mechanism of phase mixing. Local strains can exceed the macroscopic strain, where some regions preferentially deform over other regions. Enough local strain may have accumulated to allow mixing of both phases to occur by grain-boundary sliding. Conversely, at too high temperature, the strength

of a rock is lower and thus the average recrystallized grain size is larger for either one phase or both, and thus no switch in deformation mechanism to diffusion creep occurs and the rock deforms homogeneously. We observe, for example, that the recrystallized grain size of olivine is somewhat larger than that of orthopyroxene outside the mixed regions (Table 1). If this contrast in grain size is exacerbated at high temperature and geological strain rates, this may explain the discrepancy between mixed-phase ultramylonites in low-temperature shear zones (9) and unmixed high-temperature sheared llerzolites (10).

Other mechanisms that could induce mixing may be cataclastic fracturing and/or chemical reactions (6, 7). In our experiments, the latter is unlikely as any chemical reactions surely would be evident in the microstructure. No phase change or melting occurred. Cataclastic fracturing cannot be ruled out entirely. Even though we were careful not to allow the differential stress to exceed the confining pressure (Goetze criterion), there is still substantial friction in the Griggs apparatus. However, the cracks seen in the microstructures can be attributed to quenching and decompression cracking and are not necessarily evidence for cataclastic fracturing.

Several samples were analyzed by EBSD techniques to determine whether fabric strength predicts a switch in deformation mechanism. We present a map of the least deformed sample GA268 in Fig. S2, and pole figures of samples GA265, GA267, GA268, and GA270 are presented in Fig. S3. The EBSD map shows, in particular, the onset of dynamic recrystallization where some large orthopyroxene grains are elongated and breaking up into smaller grains (Fig. S2). From such EBSD maps, we constructed pole figures for all samples that generally show a weak LPO for both phases ( $M$ -index  $< 0.1$ ). The olivine LPO mostly exhibit type A (010)[100] slip, and the orthopyroxene LPO exhibits in most samples (100)[001] and (010)[001] slip. Although the recrystallized grain size fraction of GA270 has the highest  $M$ -index, generally no substantial contrast in fabric strength is demonstrated between large and small grains in the samples. We suggest the following reasons to explain this observation. First, the samples (except GA270) were deformed to shear strains of  $\gamma \sim 1$ , which may not be enough strain to obtain a mature fabric, nor do pure olivine aggregates deformed in simple shear to similar strains generally show an  $M$ -index greater than 0.1 (11). Second, the deformation of large grains may have been assisted by grain-boundary sliding in the proposed diffusion creep or dislocation creep accommodated by grain-boundary sliding (Dis-GBS) regime (12), contributing to a weak lattice preferred orientation (LPO). A weak LPO is also predicted for diffusion creep in the fine-grained regions. For these reasons, we do not attempt to infer the dominant deformation mechanism in our samples solely from the fabric strength ( $M$ -index).

Finally, in some cases a layer of small olivine and orthopyroxene grains can be seen at the sample–piston interfaces (Fig. S1), which is likely a result of higher than average stress concentrations on the hard alumina. Although the fine-grained bands are not exclusive to the sample–piston interfaces (Fig. S4D), it is possible that the irregular (serration) geometry of the sample–piston interface might have contributed to initiate shear localization. However, the influence of interface is unlikely to be large because the presence or absence of localization is related to temperature. Similarly the melt segregation in the experiments by Holtzman et al. (2003) (13) were performed using a similar sample assembly, yet the presence or absence of melt segregation and resultant weakening is not attributed to the interface geometry.

**Modeling. Construction of the rheological weakening diagrams.** The conditions for shear localization (likely associated with rheological weakening) caused by dynamic recrystallization were examined by Karato (2008) (14). In this model, two aspects of microscopic processes are considered. First, in order for shear localization to

occur by grain-size reduction via dynamic recrystallization, the size of grains formed by dynamic recrystallization must be smaller than the critical size below which diffusion creep dominates. If this condition is satisfied, then fine-grained regions (along preexisting grain boundaries) will be deformed by diffusion creep. However, grain growth in these regions will slow down the rate of deformation and eventually bring grain size close to the critical size between dislocation and diffusion creep and rheological weakening will stop (15). Therefore, the second condition that needs to be met for localization is that the rate of grain growth is sufficiently slow compared with deformation by diffusion creep. Third, the fine-grained regions need to be interconnected to control bulk rheology (16). Karato (2008) (14) formulated these processes and analyzed the conditions for rheological weakening in terms of two nondimensional parameters,  $\zeta$  and  $\xi$ , where  $\zeta = \left(\frac{d}{d_0}\right)^m > 1$  and where  $\xi = 3kd^m/\alpha Ad_0^q$ .

Here  $d$  is the critical grain size at the boundary between grain-size-insensitive (dislocation creep) and grain-size-sensitive deformation (diffusion creep),  $d_0$  is the recrystallized grain size,  $m$  is the grain size exponent, and  $k$  is the rate constant for grain growth in the form  $d^q - d_0^q = kt$ . The constant  $\alpha$  is a non-dimensional parameter of order unity and  $A = \dot{\varepsilon}_{\text{diff}} d^m$ . Localization requires larger strain development in regions that deform by diffusion creep relative to regions that deform by dislocation creep (that is, the condition  $\dot{\varepsilon}_{\text{diff}}/\dot{\varepsilon}_{\text{disl}} \gg 1$ ). This condition is controlled by recrystallized grain-size and by grain-growth kinetics.

Karato (2008) (14) thus expressed the condition for localization in terms of  $\zeta$  and  $\xi$  as:

$$\frac{\zeta(1 + \xi)^{(1-m/q)} - 1}{\xi(1-m/q)} \gg 1 \quad [\text{S1}]$$

for  $q \neq m$  and

$$\frac{\zeta}{\xi} \log(1 + \xi) \gg 1 \quad [\text{S2}]$$

for  $q = m$ .

We redefine the variables ( $\zeta$ ,  $\xi$ ) in the above expression in terms of olivine flow law parameters as follows:

$$\zeta = \frac{A_{\text{diff}}}{A_{\text{disl}}} \frac{1}{d_0^m} \sigma^{(1-n)} \exp\left(\frac{H_{\text{disl}}^* - H_{\text{diff}}^*}{RT}\right) \quad [\text{S3}]$$

and

$$\xi = \frac{3}{d_0^q} \frac{k_0}{A_{\text{disl}}} \sigma^{-n} \exp\left(\frac{H_{\text{disl}}^* - H_{\text{gg}}^*}{RT}\right), \quad [\text{S4}]$$

with a paleopiezometer of the form  $d_0 = C\sigma^{-p}$ . Flow law parameter values are given in Table S1 and the grain-growth kinetics parameters used in the model are given in Table S2.

The transition from homogeneous deformation to localized deformation, likely associated with weakening (Eq. S1 and Eq. S2), is characterized by an upper temperature boundary and a lower temperature boundary in temperature–stress space (Fig. 4). Although the upper boundary depends on recrystallized grain size, only the lower boundary is directly sensitive to grain-growth kinetics. If grain-growth kinetics is sluggish, the regime for localized deformation expands downward in temperature. However, the expansion is limited by a critical low temperature when not enough strain can be accumulated in a given timescale to develop a connective fine-grained volume fraction to cause

weakening. We assume a critical timescale for subduction of  $\sim 10$  Ma and a minimum strain of 30% (equivalent to a strain rate of  $\sim 10^{-15} \cdot \text{s}^{-1}$ ).

The model is capable to distinguish one region in temperature–stress space where localization may occur (due to phase mixing, for instance) from another region where deformation is largely homogeneous. Moreover, the model seems to fit our experiments under laboratory conditions at relatively high strain rates and temperatures, and the model fits the development of shear zones (ultramylonites) at lower temperatures ( $\sim 973$  K), likely associated with long-term weakening at geological conditions. However, the model is only valid for geological conditions if there is an addition of a second phase to reduce grain growth of olivine (Fig. 4). The weakening observed in pure olivine aggregates in the laboratory that is not associated with strain localization is likely not sufficient over geological time, nor would fast grain growth be prevented by second-phase pinning during periods of tectonic relaxation.

1. Ohuchi T, Karato S, Fujino K (2011) Strength of single-crystal orthopyroxene under lithospheric conditions. *Contrib Mineral Petro* 161(6):961–975.
2. Hansen LN, Zimmerman ME, Kohlstedt DL (2011) Grain boundary sliding in San Carlos olivine: Flow law parameters and crystallographic-preferred orientation. *J Geophys Res, B, Solid Earth* 116(8).
3. Holyoke CW, Kronenberg AK (2010) Accurate differential stress measurement using the molten salt cell and solid salt assemblies in the Griggs apparatus with applications to strength, piezometers and rheology. *Tectonophysics* 494(1–2):17–31.
4. Paterson MS (1982) The determination of hydroxyl by infrared adsorption in quartz, silicate glasses and similar materials. *Bulletin de Mineralogie* 105(1):20–29.
5. Linckens J, Herwigh M, Müntener O, Mercalli I (2011) Evolution of a polymimetic mantle shear zone and the role of second phases in the localization of deformation. *J Geophys Res* 116, 10.1029/2010JB008119.
6. Kruse R, Stünitz H (1999) Deformation mechanisms and phase distribution in mafic high-temperature mylonites from the Jotun Nappe, southern Norway. *Tectonophysics* 303(1–4):223–249.
7. Kilian R, Heilbronner R, Stünitz H (2011) Quartz grain size reduction in a granitoid rock and the transition from dislocation to diffusion creep. *J Struct Geol* 33(8):1265–1284.
8. Hellmann P, Hillert M (1975) On the effect of second-phase particles on grain growth. *Scandinavian Journal of Metallurgy* 4:211.
9. Toy VG, Newman J, Lamb W, Tikoff B (2010) The role of pyroxenites in formation of shear instabilities in the mantle: Evidence from an ultramafic ultramylonite, Twin Sisters massif, Washington. *J Petrol* 51(1–2):55–80.
10. Skemer P, Karato SI (2008) Sheared Iherzolite xenoliths revisited. *J Geophys Res, B, Solid Earth* 113(7).
11. Jung H, Katayama I, Jiang Z, Hiraga T, Karato S (2006) Effect of water and stress on the lattice-preferred orientation of olivine. *Tectonophysics* 421:1–22.
12. Hirth G, Kohlstedt DL (1995) Experimental constraints on the dynamics of the partially molten upper mantle 2. Deformation in the dislocation creep regime. *J Geophys Res* 100:15,441–15,449.
13. Holtzman BK, Groebner NJ, Zimmerman ME, Ginsberg SB, Kohlstedt DL (2003) Stress-driven melt segregation in partially molten rocks. *Geochem Geophys Geosyst* 4(5).
14. Karato S (2008) *Deformation of Earth Materials: An Introduction to the Rheology of Solid Earth* (Cambridge Univ Press, New York).
15. Drury MR (2005) Dynamic recrystallization and strain softening of olivine aggregates in the laboratory and the lithosphere. *Geological Society Special Publications* 243:143–158.
16. Handy MR (1994) Flow laws for rocks containing 2 nonlinear viscous phases—A phenomenological approach. *J Struct Geol* 16(3):287–301.

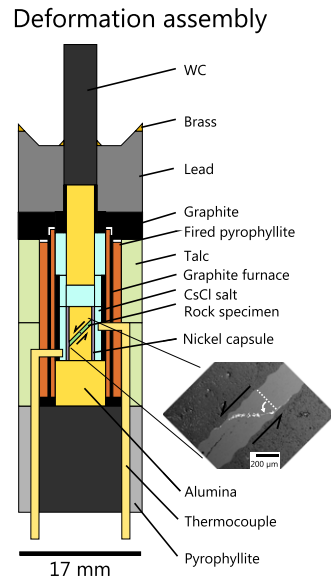


**Fig. S1.** The Griggs deformation cell modified with a CsCl solid-salt cell after Ohuchi et al. (2011) (1). The specimen is sandwiched at  $45^\circ$  between two grooved alumina pistons inside a Ni capsule and surrounded, except from below, by the soft pressure medium CsCl. The electron micrograph demonstrates the lateral movement of the pistons in  $45^\circ$  geometry, shearing the rock as indicated by the rotation of the Ni strain marker in white. For instance, a  $45^\circ$  rotation of the marker suggests a shear strain of  $\gamma = 1$  occurred under constant strain rate at high pressure and temperature.

1. Ohuchi T, Karato S, Fujino K (2011) Strength of single-crystal orthopyroxene under lithospheric conditions. *Contrib Mineral Petro* 161(6):961–975.

The model has certain limitations. It is based on simple olivine flow laws. The assumed grain-growth kinetics is based on static growth in olivine and in the mixture, whereas dynamic grain growth under deformation conditions is poorly known. For simplicity, the model calculates a sharp boundary for only one recrystallized grain size,  $d_0$ , for each (maximum) stress.

**Corrections for water loss.** Water loss occurred during the experiments, which may suggest final stresses would be lower if no water had escaped. However, detailed analysis suggests that most water was lost during the first couple of hours of annealing at target temperature (Fig. S8). Nonetheless, we investigated two cases: one where water loss was linear with time and one where water loss was logarithmic with time. Note that several key deformation experiments (GA265, GA267, GA268, and GA270) were cut from the same hot-pressed sample and thus have similar starting water contents. We recalculated the stresses for each case assuming standard olivine flow laws with  $f_{\text{H}_2\text{O}}$  dependence and show that in most cases the uncorrected stresses are not substantially different from the corrected stresses (Fig. S8).

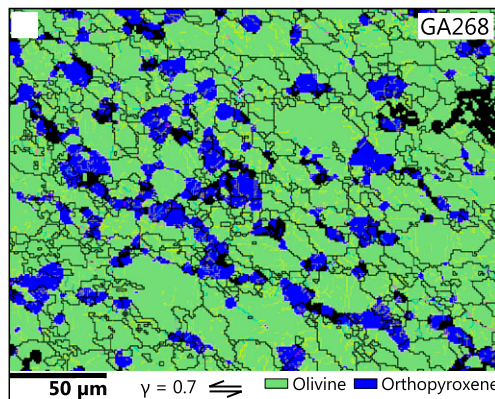


**Fig. S2.** EBSD mapping and pole figures determined for GA268 at the onset of weakening. The map was processed using noise filters for misorientations and misindexing. The black lines are high-angle ( $>10^\circ$ ) grain boundaries. The grains are colored by phase (green, olivine; blue, orthopyroxene).

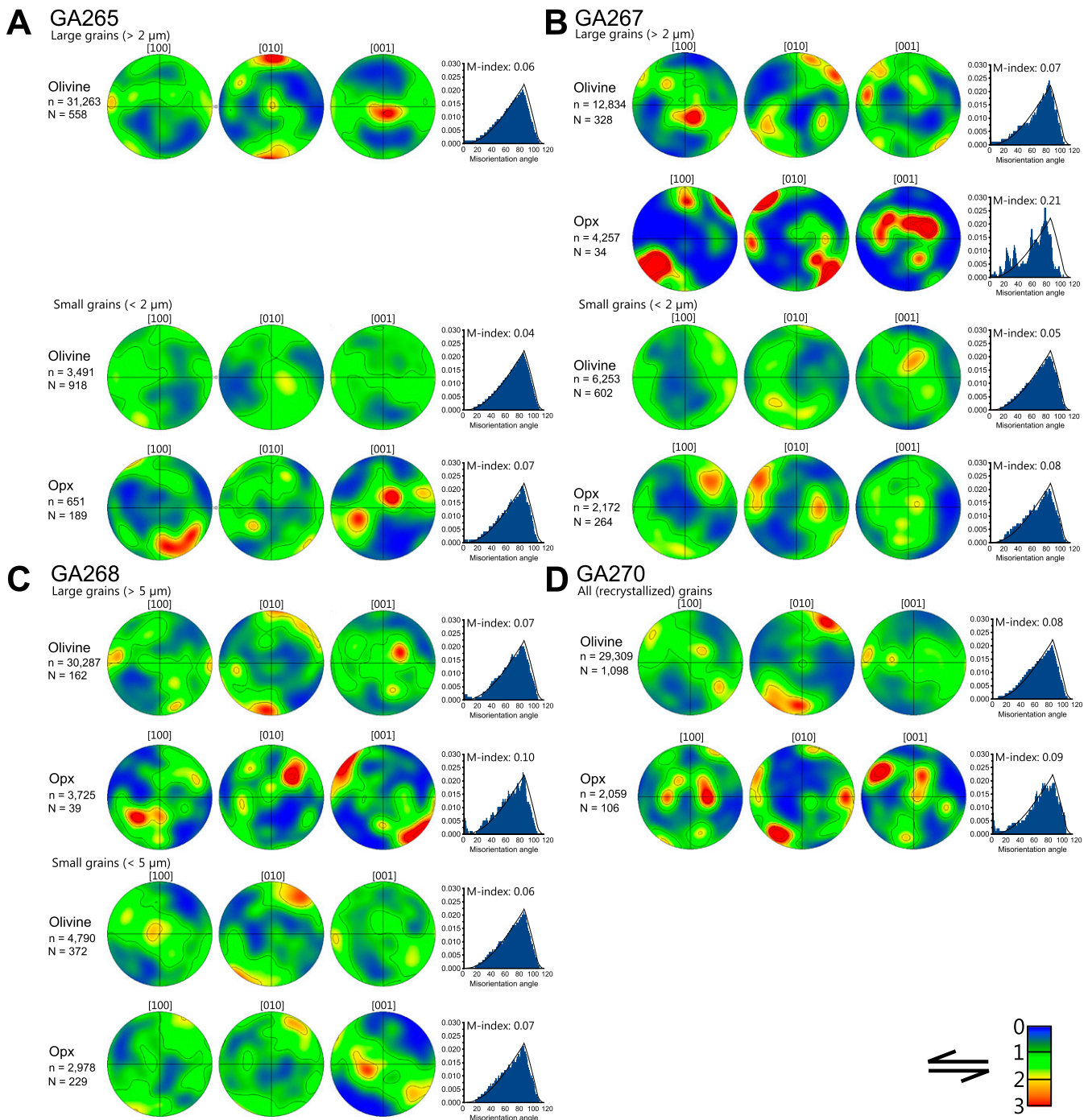


**Fig. S3.** Pole figures of grain orientations of olivine and orthopyroxene presented in sample coordinate space for [100], [010], and [001] directions. Panels A–D show the EBSD data for samples GA265, GA267, GA268, and GA270, in this order. All indexed points in each grain were included (i.e., the pole figures are weighted for grain size). East–west is the shear direction, and north–south is the normal to the shear plane. Here,  $n$  is the number of indexed points and  $N$  is the number of grains. A measure of fabric strength is given by the M-index and misorientation histograms of a random number ( $\sim 1,000,000$ ) of uncorrelated grains. The color gradient in all pole figures is normalized to multiples of uniform distribution of 3 (see legend in the bottom right corner).

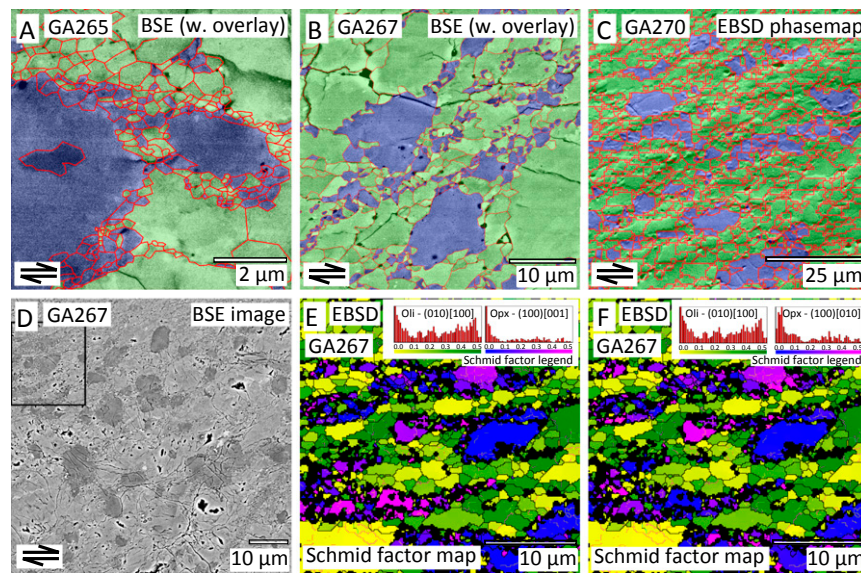


**Fig. S4.** Complementary microstructures to Fig. 2 showing some of the regions in different samples that were used for microstructural analysis (grain size, Zener pinning, grain shape, and Schmid orientation factor). *A* and *B* are BSE images of regions in GA265 and GA267 with manual interpretation of grains (boundaries were manually traced with help from stage-tilted SE images, whereas dark grains in BSE were interpreted as orthopyroxene). Olivine is colored in green and orthopyroxene in blue. *C* is a noise-reduced EBSD map of a representative region in sample GA270. *D–F* show a region in GA267 that was analyzed with EBSD techniques for phase and Schmid factor for one slip system in olivine and two slip systems in orthopyroxene.

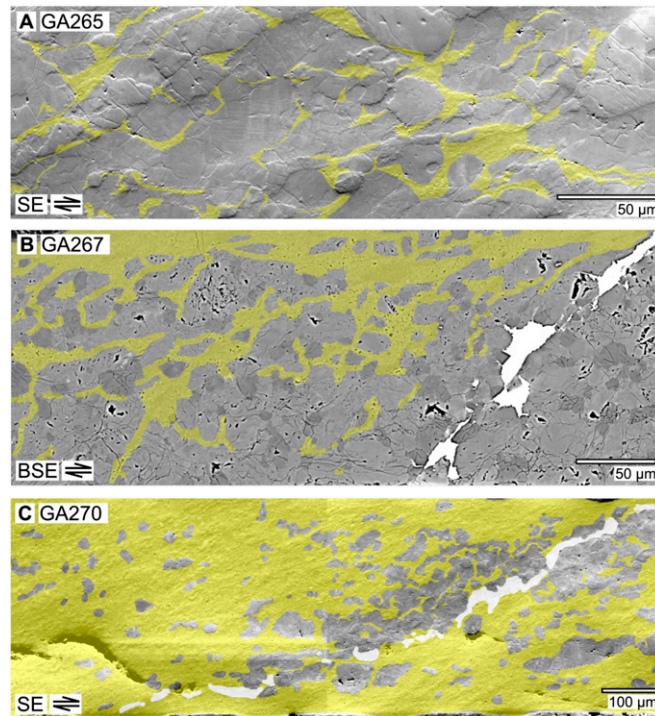


**Fig. S5.** Lower magnification SEM micrographs showing microstructures in three deformed specimens, GA265 (1,373 K), GA267 (1,473 K), and GA270 (1,540 K). The regions shaded in yellow roughly correspond to the recrystallized grains fraction. *A* and *C* are shown in SE mode, whereas *B* is shown in BSE mode (highlighting the orthopyroxene grains in darker gray).

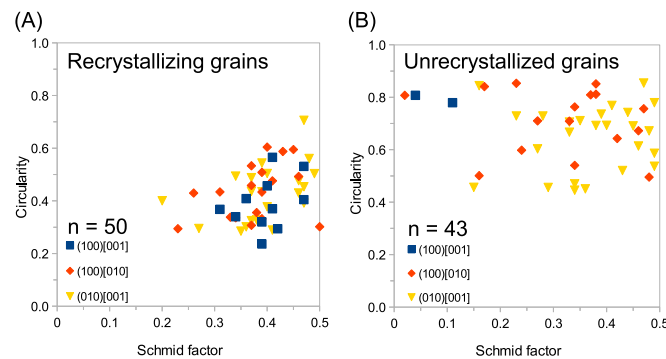


**Fig. S6.** Plots of circularity,  $4\pi(\text{Area}/\text{Perimeter}^2)$ , against Schmid factor on three orthopyroxene slip systems for highly recrystallizing orthopyroxene grains (A) and unrecrystallized grains (B). Only the maximum Schmid factor is shown for the slip system and it is highest in each grain. That is, if the Schmid factor is high for one slip system in a grain, invariably the Schmid factors for the other slip systems must be lower (which are not shown). Circularity is used to describe grain shape, where a value of 1 is a perfect circle and 0 is an infinitely long ellipse. Here  $n$  denotes number of analyzed grains per population.

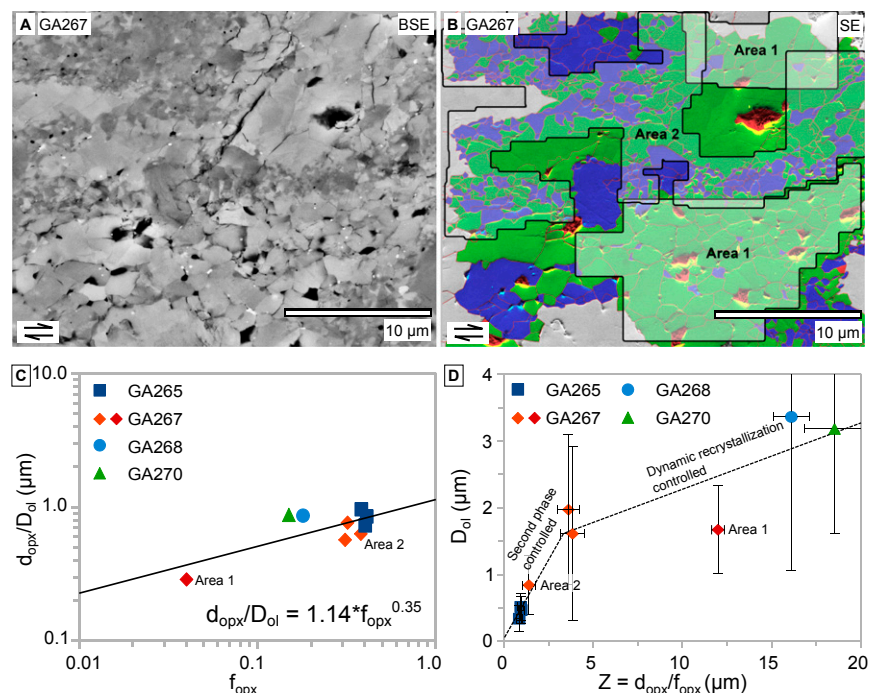


**Fig. S7.** Grain size analysis of several regions in samples to study the conditions of Zener pinning. A and B show the process of grain analysis by shape and phase. Different regions of recrystallized grains were identified as monophase (area 1) and polyphase (area 2). These areas are identified by labels on the plotting symbols in C and D. C shows second-phase grain size ( $d_{\text{opx}}$ ) divided by the olivine grain size ( $D_{\text{ol}}$ ) against second-phase volume fraction ( $f_{\text{opx}}$ ). The data are fitted by an equation with a power of 0.35 on  $f_{\text{opx}}$ . D shows olivine grain size ( $D_{\text{ol}}$ ) versus Zener parameter ( $d_{\text{opx}}/f_{\text{opx}}$ ). The data are fitted by two slopes. The change in slope suggests a change in mechanism from second-phase control (intermediate temperatures) to dynamic recrystallization control (highest temperatures and/or low strain).

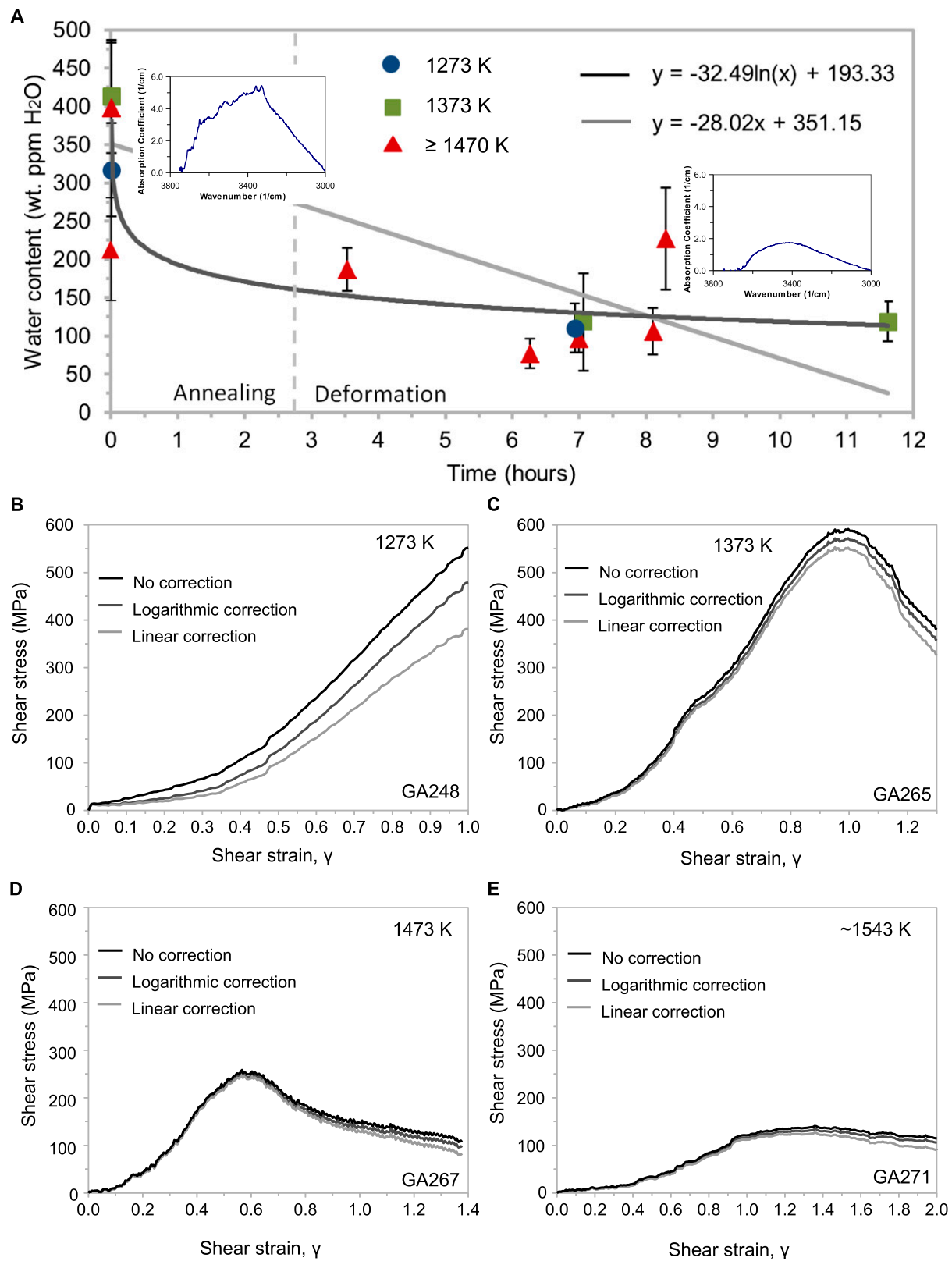


**Fig. S8.** Water loss evolution of the hot-pressed and deformed specimens. The water content of each specimen is plotted against time in A. There is no apparent temperature dependence on the rate of water loss. The error bars represent 1 SD in water content based on five or more measurements at different locations. The data points are fitted by two functions: a linear best fit and a logarithmic best fit to quantify the progression of water loss during the course of the experiments. B–E show the effect of linear, logarithmic, and no water loss corrections. Because the data indicate that water content stabilized in the samples before deformation, we did not apply any correction to the rheological data in Fig. 1.

**Table S1.** Flow law parameters used to construct deformation mechanism maps (wet rheology, Fig. 3) and model (dry rheology, Fig. 4)

Olivine flow law	$A, \text{Mpa}^{-n} \cdot \mu\text{m}^m \cdot \text{s}^{-1}$	n	m	r	$E_a, \text{kJ/mol}$	$V^*, 10^{-6} \cdot \text{m}^3 \cdot \text{mol}^{-1}$
Wet dislocation creep <sup>†</sup>	$10^{2.9(0.1)}$	3.0(0.1)	0	1.2(0.1)	470(40)	24(3)
Wet diffusion creep <sup>‡</sup>	$10^{7.4}$	1	3	0.85(1.5)	375(75)	10(10)
Dis-GBS creep <sup>§</sup>	$10^{4.8(0.8)}$	2.9(0.3)	0.7(0.1)	(1.2+0.85)/2	445(20)	18
Dry dislocation creep <sup>†</sup>	$10^{6.1(0.2)}$	3.0(0.1)	0	—	510(30)	—
Dry diffusion creep <sup>‡</sup>	$10^{9.2}$	1	3	—	375(50)	—

Flow laws are in the form:  $\dot{\varepsilon} = A \sigma^n d^{-m} f_{H_2O} \exp(-(E_a + PV^*)/RT)$ . Note that uncertainty in r is correlated with uncertainty in  $V^*$  (given in parentheses, 1 SD).

<sup>†</sup>After Karato and Jung (2003) (1).

<sup>‡</sup>After Hirth and Kohlstedt (2003) (2).

<sup>§</sup>After Hansen et al. (2011) (3).

1. Karato S, Jung H (2003) Effects of pressure on high temperature dislocation creep in olivine. *Phil Mag* 83:3401–414.

2. Hirth G, Kohlstedt DL (2003) *Rheology of the Mantle Wedge. Inside the Subduction Factory*, Geophysical Monograph Series, eds Eiler J (American Geophysical Union, Washington, DC), Vol 138, pp 83–105.

3. Hansen LN, Zimmerman ME, Kohlstedt DL (2011) Grain boundary sliding in San Carlos olivine: Flow law parameters and crystallographic-preferred orientation. *J Geophys Res, B, Solid Earth* 116(8).

**Table S2.** Grain-growth kinetics parameters

Material	$H_{gg}, \text{kJ} \cdot \text{mol}^{-1}$	q	$k_0, \mu\text{m}^q \cdot \text{s}^{-1}$
Pure olivine <sup>†</sup>	200	2	607
Mixture (75% ol + 25% opx) <sup>‡</sup>	300 <sup>§</sup>	4	497075

Grain-growth kinetics is expressed as  $d^q - d_0^q = kt$ , where  $k = k_0 \exp(H_{gg}/RT)$ .

<sup>†</sup>After Karato (2008) (1).

<sup>‡</sup>After Hiraga et al. (2010) (2).

<sup>§</sup>After Tasaka et al. (2013) (3).

1. Karato S (2008) *Deformation of Earth Materials: An Introduction to the Rheology of Solid Earth* (Cambridge Univ Press, New York).

2. Hiraga T, Tachibana C, Ohashi N, Sano S (2010) Grain growth systematics for forsterite ± enstatite aggregates: Effect of lithology on grain size in the upper mantle. *Earth Planet Sci Lett* 291(1–4):10–20.

3. Tasaka M, Hiraga T, Zimmerman M (2013) Influence of mineral fraction on the rheological properties of forsterite + enstatite during grain size sensitive creep 2: Deformation experiments. *J Geophys Res*, 10.1002/jgrb.50284.